Title: Beyond the First Tipping Points of Southern Hemisphere Climate

Author Names: 1 Terence J. O'Kane, 2 Jorgen S. Frederiksen, 3 Carsten S. Frederiksen and 4 Illia Horenko

Affiliations / Addresses
1: CSIRO Environment, Battery Point, 7004, Tasmania, Australia; terence.okane@csiro.au
2: CSIRO Environment, Aspendale, 3195, Victoria, Australia; jorgen.frederiksen@csiro.au
3: CSIRO Environment, Aspendale, 3195, Victoria, Australia; carsten.frederiksen@csiro.au
4: Faculty of Mathematics, Rhineland-Palatinate Technical University of Kaiserslautern-Landau, Kaiserslautern 67663, Germany; horenko@mathematik.uni-kl.de

This paper is a non-peer reviewed preprint submitted to EarthArXiv.
This paper is under peer review and consideration by MDPI Climate.

Article

Beyond the First Tipping Points of Southern Hemisphere Climate

Terence J. O'Kane,*, Jorgen S. Frederiksen, Carsten S. Frederiksen, and Illia Horenko,

[1] CSIRO Environment, Battery Point, 7004, Tasmania, Australia; terence.okane@csiro.au
[2] CSIRO Environment, Aspendale, 3195, Victoria, Australia; jorgen.frederiksen@csiro.au
[3] CSIRO Environment, Aspendale, 3195, Victoria, Australia; carsten.frederiksen@csiro.au
[4] Faculty of Mathematics, Rhineland-Palatinate Technical University of Kaiserslautern-Landau, Kaiserslautern 67663, Germany; horenko@mathematik.uni-kl.de
* Correspondence: terence.okane@csiro.au

Abstract: Analysis of observations, reanalysis and model simulations, including via machine learning methods specifically designed for regime identification, have revealed changes in aspects of the Southern Hemisphere (SH) circulation and Australian climate and extremes over the last half century that point to transitions to new states. In particular, our analysis shows a dramatic shift in the metastability of the SH climate occurred in the late 1970s, associated with a large scale regime transition in the SH atmospheric circulation with systematic changes to the subtropical jet, blocking, zonal winds and storm tracks. Analysis via nonstationary clustering reveals a regime shift was coincident with a sharp transition to warmer oceanic sea surface temperatures and increased baroclinicity in the large scales of the Antarctic Circumpolar Circulation (ACC), extending across the whole hemisphere. At the same time, the background state of the tropical Pacific thermocline shoaled, leading to increased likelihood of El Niño events. These changes in the dynamics have preceded additional regional tipping points associated with reductions in mean and extreme rainfall in South-west Western Australia (SWWA) and streamflow into Perth dams, and also with increases in mean and extreme rainfall over Northern Australia since the late 1970s. The drying of South-eastern Australia (SEA) occurred against a background of accelerating increases in average and extreme temperatures across the whole continent since the 1990s, implying further inflection points may have occurred. Through climate model simulations capturing the essence of these observed shifts our analysis indicates these systematic changes will continue into the late 21st century under high greenhouse gas emission scenarios. Here we review two decades of work, revealing for the first time, that tipping points characteristic of first and second order regime transitions are inferred to have already occurred in the SH climate system.

Keywords: climate change; atmospheric circulation; ocean circulation; storms; blocking; regimes; informatics

Citation: O'Kane, T.J.; Frederiksen, J.S.; Frederiksen, C.S.; Horenko, I. Beyond the First Tipping Points of Southern Hemisphere Climate. *Climate* **2023**, *1*, 0. https://doi.org/

Received:
Revised:
Accepted:
Published:

1. Introduction

The severe risk of potential tipping points in regional and global climate under global warming has been emphasized in a number of recent studies [1–4] and the recent report *The Risks to Australia of a* 3°C *Warmer World)* (2021) by the Australian Academy of Science [5]. The aforementioned studies detail important regime transitions of the earth system that, if they were to occur, would be catastrophic leading to a markedly less habitable future global climate. Interactions and reinforcements of regional tipping points, in particular excedence of warming thresholds, are already evident and impacting phenomena at high latitudes including Greenland ice sheet loss, Arctic sea-ice reduction, acceleration of Antarctic ice sheet loss and Siberian permafrost thawing [2]. Polar ice loss will inevitably lead to global impacts such as sea level rise - and has the potential to lead to a slowdown of the Atlantic deep ocean circulation through freshwater injection. Additional regional impacts at lower latitudes are already evident in the die-off of coral reefs and increased frequency of droughts and forest fires.

There is evidence that changes in aspects of Australian climate are sufficiently remarkable that regional regime transitions have already occurred [6]. Our purpose here is to review and collate the authors' and their collaborators work describing hemispheric shifts in the Southern Hemisphere (SH) atmospheric and oceanic circulations and to place the observed regional changes within the context of regime transitions in the background circulation. In doing so, we show that the inferred hemispheric circulation changes are dynamically consistent and are the primary causes of the regional regime transitions, indicating that hemispheric critical points have been exceeded. Moreover, skilful climate models predict that the trends that have occurred over the 20th and early 21st century will continue into the late 21st century under high emission scenarios. All of these results provide evidence that aspects of the SH climate system, and Australian climate in particular, have transitioned beyond the first tipping points. The purpose here is to describe manifestations of regime shifts in the atmosphere, ocean and sea ice, their changing dynamics and causes as elucidated in observational and model data via nonstationary Granger causal [7,8] machine learning methods, and instability calculations.

It is important to note that it is difficult to detect systematic spatio-temporal changes in the features of persistent coherent states under the influence of external covariates (radiative forcing) using analysis and/or machine learning methods where statistical stationarity is assumed. In such analysis, the underlying system's nonstationarity effectively reduces the sample size statistics that could be considered as at least locally-stationary, therefore resulting in a classical "small data" problem. Parametric detrending, for example via application of regression or a spline, prior to applying popular machine learning tools e.g., k-means clustering, neural networks, EOF/PCA, to nonstationary data may lead to biased results since such time series data can violate the underlying parameter stationarity assumption inherent to those common tools. For example, training a neural network on historical records results in obtaining fixed parameters i.e., weights and biases, that are time independent and do not change over the whole training interval. Where the neural network is trained on model simulations, the (climate) model biases are inherited by the machine learning process. As a consequence, such *parametric* tools have difficulties discerning nonstationary regime transitions between metastable states from relatively short and noisy observational data sequences [9–12].

To address the intrinsic nonstationarity, in the regime analyses presented here we deploy a *nonparametric* nonstationary clustering methodology that has been shown to be successful in analysis of highdimensional time series data with relatively short statistics length and high levels of noise - across a broad class of problems ranging from molecular and fluid mechanics, geosciences, economics and biomedicines. Specifically, we apply the nonparametric finite element bounded variation vector auto-regressive with external factors method (FEM-BV-VARX: [13–16] and described in the appendix A) to nonstationary gridded climate reanalysis and simulation data. Complementary methods based on instability calculations and decomposition are further employed to better understand the past changes in the circulation and future trends.

2. SH Atmospheric Circulation

Over the six decades between 1948-2009, systematic changes in the baroclinicity of the subtropical jets and their impact on regional precipitation trends over Southern Australia occurred against a hemispheric regime transition in the large scale flow. Specifically, large changes in SH storm track modes have occurred in all seasons including the austral winter, when blocking is at its most active [17]. The austral winter storm track changes manifest as reduced baroclinicity and a decrease in the July zonal winds of about $10ms^{-1}$ in the subtropical jet relative to the earlier period 1949-1968 [18]. The changes in the storm track modes provide a dynamical mechanism for the observed systematic linear downward trends in the annual number of SH blocking events [15,19]. Such events, predominantly occur in preferred locations about the Australian (110°E-210°E); eastern Pacific (260°E-315°E); and Indian (20°E-80°E) ocean sectors. These regions are associated with the ridges of the hemispheric wave-3 pattern [20,21]. Specifically, the transition to a dominant Southern Annular Mode (SAM) i.e., the teleconnection pattern which characterizes a largely zonal state, and a weakening of the SH wavenumber 3 teleconnection pattern, which is associated with the three major regions of tropospheric blocking. Applying a data-driven methodology to atmospheric reanalyses, O'Kane et al. (2013) [15] first determined time series of the prevalence of wave number 3 blocking states and the more zonal positive SAM states over the last 60 years. They found systematic trends in the dynamics of the troposphere reflecting a marked decline in SH mid-latitude blocking (wave-3) over the post 1978 period accompanied by a strong trend to one biased toward the positive phase of the zonal SAM state consistent with a more "summer-like" midlatitude circulation [22,23]. In contrast, prior to the 1950s and 60s, the flow was largely characterised by transitions between a dominant positive wave 3 teleconnection (enhanced blocking in the Tasman Sea and close to South Africa and Patagonia) and its sub-dominant negative phase (enhanced zonal flow in the Tasman Sea and close to South Africa and Patagonia). However, from late 1960 these preferred states underwent systematic changes whereby the positive wave-3 state occurred less and less frequently as the westerly zonal jet intensified and moved poleward. Over the same period, the negative wave-3 phase became increasingly zonal and more frequent until ultimately evolving into the dominant positive SAM phase associated with the increasingly strong polar jetstream westerlies observed over the most recent decades. These cluster results broadly agree with the changes in the zonal winds documented in the earlier instability calculations of Frederiksen and Frederiksen [18,24,25]. In particular, Frederiksen et al. [18,25] showed decreases in subtropical jet strength, reduced growth rates of mid-latitude blocks as well as extratropical storms, after the mid-1970s were coincident with the SAM being strongly correlated with increases in the polar jet strength. These results on the reduction of winter storm formation over Australia after the mid-1970s have also been confirmed in the data study of Osbrough and Frederiksen (2023)[26].

While an early study hypothesized that global warming is likely to change the frequency of occurrence of these circulation regimes but not their spatial patterns [27], the aforementioned studies reveal that the spatial character of the SH persistent climate regimes has indeed changed significantly over the period 1948-2009. As we discuss in detail in section 2.2, Franzke et al. (2015) subsequently conducted a formal attribution study to determine the relative role of anthropogenic greenhouse gas concentrations and other radiative forcing in driving observed changes in the large-scale circulation of the SH troposphere. They found CO2, and to a lesser degree the seasonal impact from stratospheric ozone, to be the dominant driver(s) of the observed systematic circulation changes. They also found that reduced temperatures associated with emission of sulphate aerosols from particularly large volcanic eruptions allowed the positive wave-3 blocking state to temporarily re-establish as the dominant meta-stable state.

In the following sections we examine the 1980s climate regime transition with a particular focus on the Pacific where the impacts of the changed dynamics are most evident.

2.1. Sectorial Trends in the Frequency of Occurrence and Persistence of Synoptic Structures

O'Kane et al. (2013) [15] revealed evidence for significant secular trends in persistent circulation regimes associated with SAM and a hemispheric wave-3 blocking pattern in all seasons. Subsequent examination [22] of secular trends in the time of residence in either a wave-3 blocked or zonal (positive SAM) state found that the observed increasing frequency and persistence of positive SAM pattern is accompanied by a corresponding decrease in the frequency and persistence of the wave-3 hemispheric pattern, which features blocking in the Australian, South American and South African sectors. In an examination of JRA-55 reanalysis data [28], O'Kane et al. (2016) [23] reported the hemispheric regime transition previously observed in NOAA NCEP reanalysis 1 [29] also manifested in the late

1970s–early 1980s with similar correspondingly stronger zonal flows in the region to the south of the Australian mainland and a general reduction in baroclinic instability in the subtropics between 90°E and 180°E. A sectoral analysis further found that, post 1980, over the western Indian Ocean and for the eastern Atlantic region to the east of South America, a significant reduction in baroclinic instability occurred coinciding with a shift to more convergent upper level winds. For the Australian–New Zealand sector between 150°W - 110°E the summer periods were dominated by significant surface air temperature anomalies over the coast of Western Australia about Perth as a result of persistent anticyclones in this node of the circumpolar waveguide. The preferred wintertime state is characterised by warm surface air temperature (SAT) anomalies, upper level divergence, strong baroclinic instabilities and the generation of Rossby waves to the south of Perth and to the southeast of Madagascar. There occurred a noticeable regime shift in the summertime circulation about 1980 in the Pacific where the summertime trends exhibit a transition from a period of relatively regular decadal variations between states to the one characterised by a significant anticyclonic 500 hPa height anomaly to the South of the Tasman Sea, anomalously warm surface air temperatures extending from Tasmania to Victoria and then inland and reduced baroclinic instability between the Australian mainland and 50°S. The annual trend indicates that the summertime circulation trends are dominant.

O'Kane et al. (2016,2017)[23,30] showed that systematic changes in the persistence and frequency of occurrence of the formation and decay of coherent atmospheric states happen throughout all four seasons. However, the trend is nearly linear throughout the summer season whereas there was observed a much more distinct regime transition during the other three seasons. We next discuss the evidence for anthropogenic greenhouse gas concentrations to be the primary driver of these secular trends.

2.2. The Transition to a Dominant Zonal Mean SAM$^+$ like Circulation Post 1978

Climate models, traditionally the main method of investigating the role of radiative forcing in the atmospheric circulation [31–36], have identified stratospheric ozone depletion as an important driver of the observed austral summertime intensification of the SAM over the recent decades. However, stratospheric ozone depletion is a highly seasonal effect and can play no role in the austral winter-spring atmospheric circulation dynamics. The SH storm tracks are equally active all year around [37]. However, the austral wintertime is the season when the observed changes to the storm track activity, namely reduced blocking and baroclinicity of the subtropical jet [18], have been particularly evident and cannot be solely attributed to the ozone mass deficit (OMD). Franzke et al. (2015) [22] chose to examine Z^{500hPa} geopotential height anomalies (seasonal cycle subtracted) projected on the 20 leading EOFs and with the external covariates in a temporally regularized VARX model in terms of various combinations of the major radiative forcings. The forcings considered were Cape Grim CO2 measurements [38], sulfate aerosols [39], stratospheric aerosol optical thickness [40], the solar constant [41], and stratospheric ozone mass deficit (OMD)[42], including accounting for the time lagged seasonal OMD impacts on the circulation. They also considered the role of the major tropical internal modes of climate variability, specifically the ENSO3.4 index, the Madden–Julian Oscillation (MJO) index, the Indian Ocean Dipole (IOD) and the eastern IOD mode indices. These indices describe tropical sea surface temperature (SST) variability (ENSO, IOD) or an intrinsic mode of tropical intraseasonal variability (MJO).

Deploying the FEM-BV-VARX method, comprehensive sensitivity tests were carried out [22] for the cluster parameters involving memory depths between 0 and 5 days, where 2 days was found to be optimal, and several choices of annealing steps between 4 and 64. Daily forcing agents were spline interpolated with no lag apart from OMD and every possible combination of forcing agents was considered including the observed OMD lagged by 0, 30, 60 and 90 days, as well as a variant with a lag average of 365 days span. The optimal external radiative forcing agent was found ultimately to correspond to the Cape Grim CO2 time series determined by application of the Akaike Information Criteria(AIC) [43]. This is equivalent to assuming that the scalar valued squared model errors are χ^2 distributed and that the vector-valued FEM-BV-VARX model errors are Gaussian. The analysis of Franzke et al . (2015) [22] found strong evidence that anthropogenic greenhouse gas concentrations are the root cause of the observed secular trends in the SAM and hemispheric wave-3 pattern. The clustering analysis with CO2 forcing found a corresponding Akaike weight of close to 1 denoting the most parsimonious explanation of the observational data among all of the other fitted explanatory statistical models with all possible combinations of radiative forcings considered and taking into account possible overfitting.

The associated metastable states and their features were seen to have very different expression and corresponding surface air temperature (SAT) signatures. The wave-3 blocked regime dominant prior to the late 1970s climate transition corresponded to a cold SAT anomaly over the Antarctic Peninsula and warm SAT anomalies over the Ross Ice Shelf, the coast of Antarctica's Victoria land and over South America. The zonal positive SAM regime was associated with a warm SAT anomaly over East Antarctica and Australia and a cold SAT anomaly along the coast of Antarctica's Wilkes Land. Examination of the trend in SAT over the same period (1979–2010) calculated from yearly averaged Had4Krig version 2.0.0 data [44], showed remarkable agreement between the dominant SAM state SAT anomaly pattern and the Had4Krig SAT trend pattern over Antarctica, providing further independent evidence of the weakening of the wave-3 blocking state. The strong trend towards the SAM state over recent decades coincides with recent reports of loss of Antarctic ice mass.

The results of Franzke et al. (2015) [22] are in contrast to earlier studies which indicated a much more dominant role to O_3 [33,42,45]. In particular the study by Roscoe and Haigh [42] attributed ozone depletion (OMD) to being up to 9 times more important than anthropogenic CO_2 concentrations in explaining these trends. Their study considered only 365 day lagged OMD where ozone is considered to act in all seasons. These studies mainly focussed on the austral summer season and the poleward shift of the Hadley cell, increasing westerly winds, and the linear trend in the zonal mean circulation towards the positive SAM phase focussing on changes in the mean state rather than the frequency of occurrence and structural changes of the synoptic features in the data. Freitas et al. (2015) [46] demonstrated that these interdecadal changes in the SH circulation could in fact be simulated with a general circulation model forced by observed SSTs and historical time-varying CO_2 concentrations. Importantly, the FEM-BV-VARX data-driven methodology represents a non-stationary extension of the Granger causal inference [7] applied to attribute changes to the entire SH circulation including time evolving systematic changes to the frequency and persistence of coherent synoptic features to all possible combinations of the relevant radiative forcings.

2.3. Weakening of the Subtropical Jet and Storm Tracks and Impact on Rainfall Over Southern Australia

Australian, and particularly South-west Western Australian (SWWA), rainfall and associated streamflow are affected by circulation features including the Indian Ocean Dipole (IOD [47]), SAM [31,48]) and to some extent the Southern Oscillation Index (SOI, [49]) and to a lesser extent various other indices including local effects such as land clearing [15,23,30,50–55]. Frederiksen et al. [18,24] found that large scale atmospheric circulation phenomena and associated changes in extratropical storms were major factors in the SWWA rainfall reductions post the 1970s. Importantly, the large scale atmospheric zonal wind changes were seen to extend around the whole SH in patterns dominated by a longitudinally symmetric component. The aforementioned studies focused on changes in the atmospheric circulation and storm tracks in terms of differences between two periods namely (1975-1994) minus (1949-1968). They showed that in the latter twenty-year period the average peak zonal wind in July, in the subtropical jet between 30°S and 35°S and between 100°E and 130°E, decreased by $9.4 ms^{-1}$ or 17% at 150 hPa representing a substantial drop in the strength of the thermodynamical engine driving the SH circulation which was reflected in

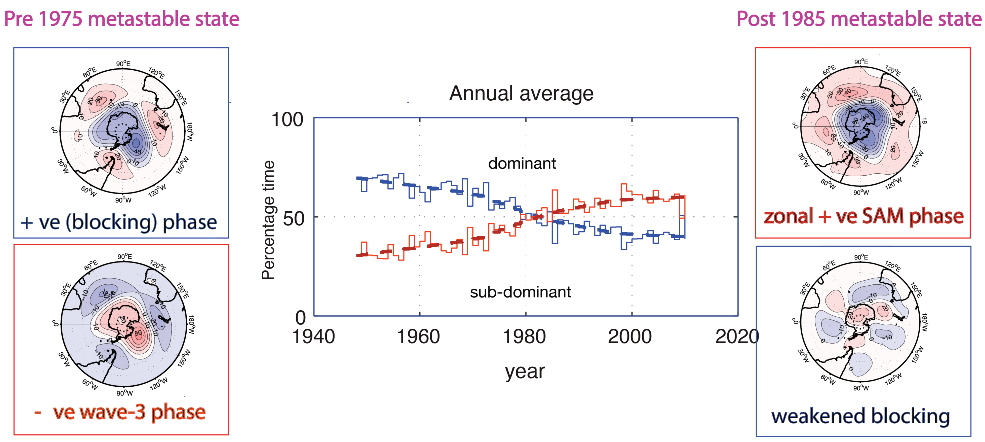

Figure 1. Regime states of 500-hPa geopotential height anomaly from NCEP reanalysis data covering the period 1948-2009 averaged over all months of the year based on the nonstationary data clustering (see appendix 1).

a circa 20% reduction in SWWA rainfall at the time. These largely zonally symmetric wind changes were further associated with a reduction in the temperature gradient between the high and middle latitudes and with an increase in the strength of SAM, and related increase in the strength of the polar jet.

Another particularly important aspect of the changes in the atmospheric circulation pre and post the mid-1970s has been the reduction in the potential for storm formation via a weakening of the subtropical jet. Frederiksen et al. [18] analysed the Phillips (1954) [56] instability criterion for SH storm development. This is a measure of the vertical shear of the zonal wind relative to a critical threshold shear, where the criterion, based on winds at 300hPa, 700hPa and the critical value, $u^{300} - u^{700} - u^{critical} > 0$ is necessary for instability leading to storm formation. Here, $u^{critical}$ depends on the vertical temperature gradient, and the Coriolis parameter which is essentially constant between the two periods. Based on reductions in baroclinicity, they showed (their figure 2) that one would expect a reduction in storm formation in the latitude band 25°S-35°S at practically all longitudes in the SH, and an increase further south. They showed that the changes in Phillips criterion for storm formation were consistent with more complex instability calculations of the growth and structures of extratropical storms affecting southern Australia. These calculations revealed that the fast-growing storms had growth rates reduced by as much as 30% in the period post 1975 compared with the earlier period. As well, some storms were deflected southward.

Frederiksen & Frederiksen (2011) [25] later documented additional changes in the major large-scale atmospheric circulation anomalies associated with changes in instability weather modes during the 10-year interval 1997-2006 at the start of the AMD. Specifically, they performed comprehensive model based instability studies of the three-dimensional circulation finding that the reduction in baroclinicity, particularly in the Australian region of the subtropical jet, resulted in reductions in the growth rate of leading storm track modes (of more than 30%) and onset-of-blocking modes (around 20%) but with increases in growth of north-west cloud band (NWCB) modes [57] and intraseasonal oscillation activity (Table 2 of [25]). Risbey et al. (2013) [58], in an observational study of synoptic components of rainfall variability in SEA, found that during the AMD the reduction in rainfall was due to fewer intense fast growing frontal storms and cut-off lows associated with the reduced baroclinicity in the subtropical jet in the Australian region and consistent

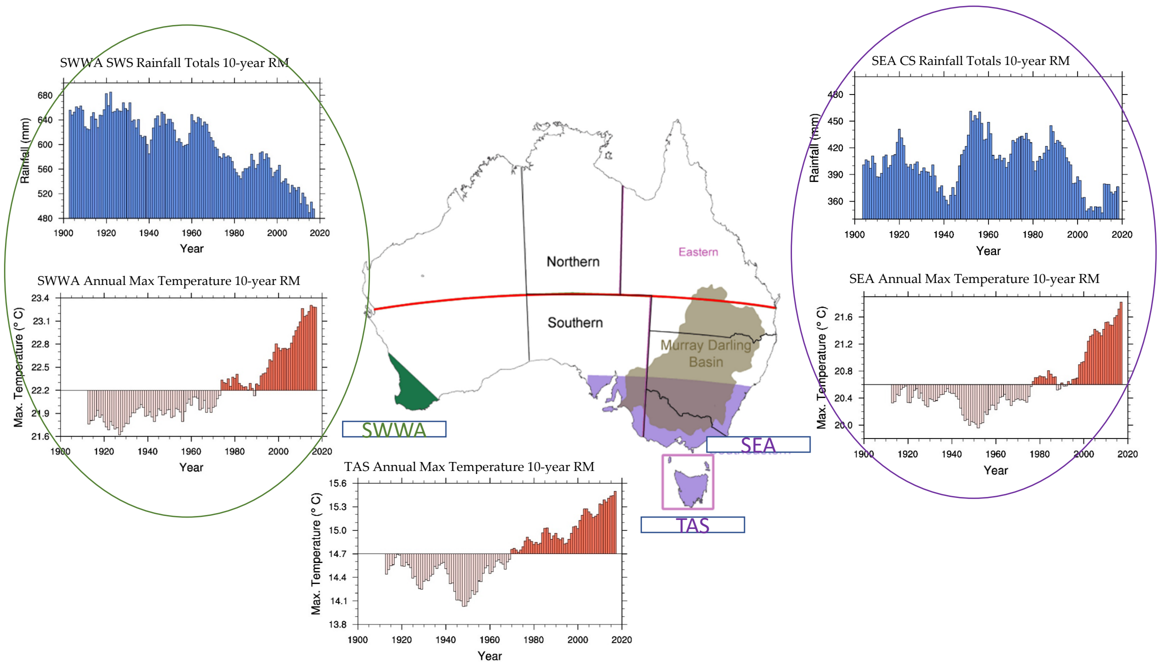

Figure 2. 10-year running mean of SWWA & SEA rainfall totals for Cool Season (CS), April to October. 10-year running mean of SWWA, SEA & Tasmanian annual maximum temperatures

with theoretical predictions ([18,25]). Compared to a base-line period 1949-1968, the zonal wind in a longitudinal belt around 30°S was reduced by as much as $8ms^{-1}$ at 300 hPa and increased by similar amounts near 55°S while at 700 hPa the corresponding changes in magnitudes were as large as $5ms^{-1}$ or more. These differences were again shown to have a zonally symmetric component but with significant peaks around the longitudes of the Australian continent. Latitude height cross sections of the zonal wind averaged between 110°E and 160°E showed a peak reduction of more than $6ms^{-1}$ near 150 hPa at 30°S and a slightly large increase peaking near 250 hPa at 55°S. Consistent anomalies occurred in the 500 hPa temperature and geopotential height and sea level pressure (Fig. 3 of [25]).

The pre and post mid-1970s changes in the hemispheric circulation and extratropical storms described for the peak austral winter season are reflected by broadly similar changes in other seasons. Frederiksen et al. (2017) [36] revealed systematic changes in all seasons, over the second half of the twentieth century, in terms of changes in the annual cycle of SH baroclinic instability. They showed significant negative trends in baroclinic instability, as measured by the Phillips Criterion, in the regions of the climatological storm tracks occurring against significant positive trends in a zonal band occurring further poleward with corresponding changes in the growth rate of storm formation at these latitudes over this period and a general preference for storm formation to be moved further poleward than had previously been the case.The weakening of the upper-troposphere jet just poleward of 30°S, with maximum reduction at circa 150 hPa, and strengthening futher south corresponded to a general decline until the late 1970s followed by annual variability but little systematic trend thereafter. These broad scale features were also seen in the zonal wind difference between 300 hPa and 700 hPa, and temperature increases accompanied by rainfall decline (see figure 2) over southeastern Australia from the mid to late 20th century [6,25,36].

3. Pacific and Southern Hemisphere Oceans

We now focus on observed widespread and systematic shifts that occurred simultaneously across the SH oceans but with a particular focus on ocean teleconnections between the tropical Pacific ocean and higher latitudes. We examine dynamic and thermodynamic

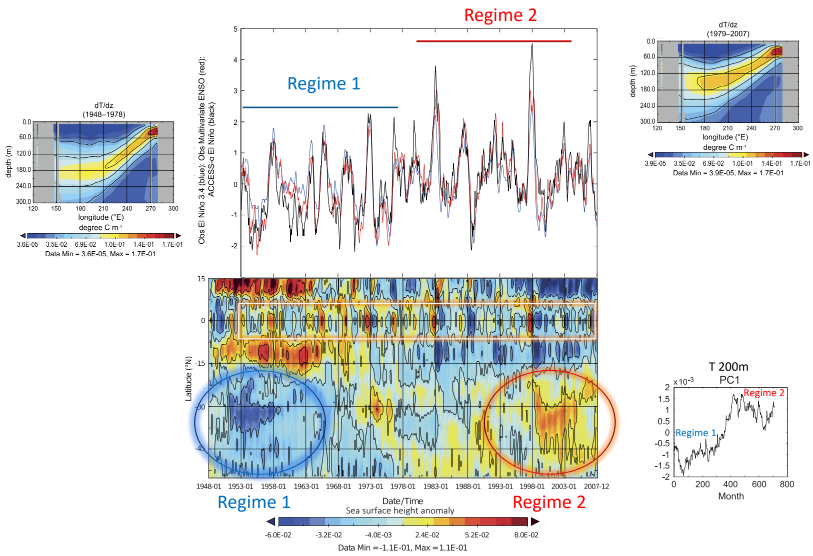

Figure 3. Comparison of the observed ENSO variability (Multivariate ENSO Index (red) and Niño3.4 Index (blue)) to the model Niño3.4 (black)). (lower) ENSO variability in modelled sea surface height anomaly in time versus latitude (15°N-52.5°S) and averaged over longitudes spanning the Pacific. The mean thermocline positions for periods (1948-1978) and (1978-2007); The leading PC1 of South Pacific Ocean (SPO) variability at 200m depth characteristic of the SAM.

internal ocean pathways and the atmospheric processes which excite these modes to form oceanic bridges connecting the tropical Pacific to the higher latitudes.

3.1. ENSO Teleconnections

Freitas et al. (2015) [46] first showed that the tropospheric circulation changes described in section 2 were coincident with to a shift to warmer sea surface temperatures (SST) in the southern oceans. In this section we examine evidence for tropical - extratropical oceanic teleconnections and the role of ENSO, and the mechanisms by which atmospheric forcing drives this shift.

In the tropics preceding a period of strong and sustained El Niño events during the late 1970s, the equatorial Pacific thermocline basic (time mean) state shoaled becoming more El Niño like. O'Kane et al. (2014)[59] described the two distinct equatorial regimes characterized as

- Regime 1 (Prior to 1978): A deepened western equatorial Pacific thermocline basic state and a more stably stratified (weakly stratified) density structure below (above) the thermocline.
- Regime 2 (Post 1978): A shallow western equatorial Pacific thermocline basic state and a more stably stratified (weakly stratified) density structure above (below) the thermocline.

The upper middle panel of figure 3 depicts the observed ENSO variability (Multivariate ENSO Index (red line) and Nino3.4 Index (blue line) from HadISST data to that simulated by a coupled ocean-sea ice model forced with bulk formulas derived from the NOAA NCEP reanalysis version 1 (black line). A regime state with generally smaller and cooler anomalies existed prior to the 1980's whose mean thermocline state, shown in the left panel insert, is given by the vertical gradient of temperature. The Hovmöller diagram (lower middle panel) of sea surface height anomalies between 15°N and 52.5°S and averaged over longitudes spanning the Pacific, shows a transition from predominantly negative anomalies with corresponding cooler surface temperatures prior to 1980 between 15°S and 52.5°S with maximum values about 30°S.

Between 1975 and 1983 the ocean underwent a transition to a new regime where the ocean thermocline basic state was shoaled with respect to the earlier period (upper right panel insert) and a number of very strong El Niño events occurred. Evident in the time series of ENSO is an enhanced low frequency component post 1980. In the subtropics and mid-latitude Pacific a new regime emerged dominated by positive height anomalies associated with a warmer surface ocean and seen in a sustained shift to warmer upper ocean temperatures (5m to 280m) in the region 70°-22.5°S, 120°E–60°W associated with the South Pacific decadal oscillation (SPDO). Using a linear inverse model framework, Lou et al. (2020) [60] show reconstructions of the low frequency SPDO variability, in both observations and simulations (figure 3) with correlations between the reconstructed SPDO and the observed or simulated SPDO of 0.81 and 0.73, respectively. They found that upper ocean temperature anomalies in the midlatitudes also exhibit low frequency regime behaviour of the type associated with the 1980s regime transition (lower right panel insert). The systematic changes to a more "El Nino-like" equatorial ocean thermocline and increased amplitude of El Niño variability also coincide with a similar shift in the variability and phase of the Interdecadal Pacific Oscillation (IPO) (figure 4) [61].

Applying nonstationary cluster analysis [62], Freitas [46] examined Pacific ocean SSTs over the time period January 1870–August 2012 from HadISST data. Retaining only the first 10 components from a EOF/PCA decomposition, the two leading cluster states (figure 4) reveal warm and cold persistent anomalous states relative to the background state. The warm state 2 corresponds to large scale warming of the southern ocean with enhanced warming of the western boundary currents—the East Australian Current, Brazil-Malvinas Confluence and the Agulhas Current. In this case, for any given data instance (monthly mean) the clustering finds the state that is most similar to the data assigning probabilities $\gamma_i(t)$ (Equations A2-A6) that the data is in a given metastable state after which a binary classification of the data associates the monthly mean HADISST data with one of either the warm or cold metastable regimes. Averaging anomalies according to $\gamma_i(t)$ shows the broad features whereas application of a 12-month digital filter to the affiliation sequence reveals trends in the data. We see that prior to about 1978 there was marked switching between states interspersed with periods of relative persistence in a given state but with no discernable preference for one state over the other. Post 1978 the system has locked into the warm state.

3.2. South Pacific Ocean Teleconnections

In the remaining sections we show how dynamical teleconnections internal to the ocean also bear the imprint of the 1980s tipping point. We begin with describing one of the longest continuous records of SSTs in the SH namely, the Maria Island time series, the imprint of the 1980s tipping point, and the mechanism by which the observed variability arises. In figure 5 we show the "ocean storm tracks" that allow large-scale baroclinically unstable waves to transverse the South Pacific subtropics within waveguides associated with potential density gradients at latitudes and depths associated with mode water formation. The pathways and mechanism by which coherent baroclinically unstable disturbances propagate and are trapped and amplified via resonant interaction with topography may be summarized from the findings of O'Kane et al. (2014)[63], thus:

- Potential energy of the large-scale mean ocean circulation is generated by the action of the large-scale mean wind field.
- This energy is converted from baroclinic (APE) to barotropic (EKE) energy in regions where subtropical mode water forms.
- The associated baroclinic disturbances are inherently nonlinear and multiscale and are amplified and or trapped through resonant interaction with topography.
- These nonlinearly modified Rossby waves are associated with persistent states that develop after the eddy wave number spectrum becomes saturated and long-wavelength coherent structures form.

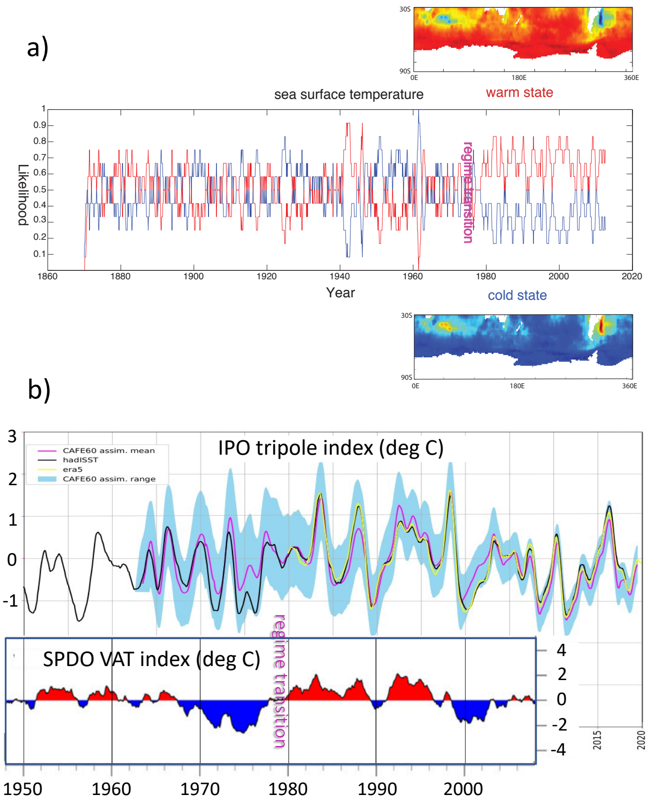

Figure 4. (a) Composite regime states of SST anomalies based on the FEM-BV-VARX cluster analysis (see appendix) of HADISST data over the region south of 30°S: values greater than 0.1 or less than -0.1 are significant at the 95 % confidence level; (centre right panel) time series of the model affiliation sequence $\gamma_i(t)$, from cluster analysis of HADISST data with 12-month digital filter applied. Blue (red) line corresponds to cold state 1 (warm state 2). (b) Timeseries of the interdecadal Pacific oscillation from HadISST, ERA5 and the CAFE60 large ensemble reanalysis which includes uncertainty estimates in terms of the ensemble spread calculated from a O(100) member ensemble Kalman filter. Subsurface South Pacific Decadal Ocean variability via vertically averaged temperature (SPDO VAT) between 5m to 280m in the South Pacific 70°-22.5°S, 120°E–60°W).

These wavelike features provide an important mechanism to communicate information on interannual time scales across the Pacific, Indian and midlatitude oceans [63,64].

In figure 5 we show a schematic describing the aforementioned waves and their pathway across the South Pacific to the east coast of Australia where they enter the East Australian Current (EAC) via the South Caledonian jet and South equatorial current [65]. Having entered the EAC these disturbances can amplify then traverse the EAC and its extension toward Maria Island or alternatively traverse the Tasman Front from near Sydney towards New Zealand. The figure panel depicting the Maria Island station SST time series data (4 year running mean) shows increasingly larger amplitudes in the low frequency variability post 1980. The models including data assimilation all display the observed variability with the assimilation models including subsurface temperature (T), salinity (S) and satellite SST data. All model variants shown are able to simulate the observed variability at Maria Island with data assimilation acting to remove systematic biases rather than impose variability. At the location of Maria Island, the model maximum of the thermocline potential temperature gradient $d\theta/dz$, the buoyancy frequency N^2 and baroclinic energy conversion Φ', here normalized, scaled and a 4 year running mean applied, are all significantly correlated with observed SST variability (p-value < 0.05). It is notable that

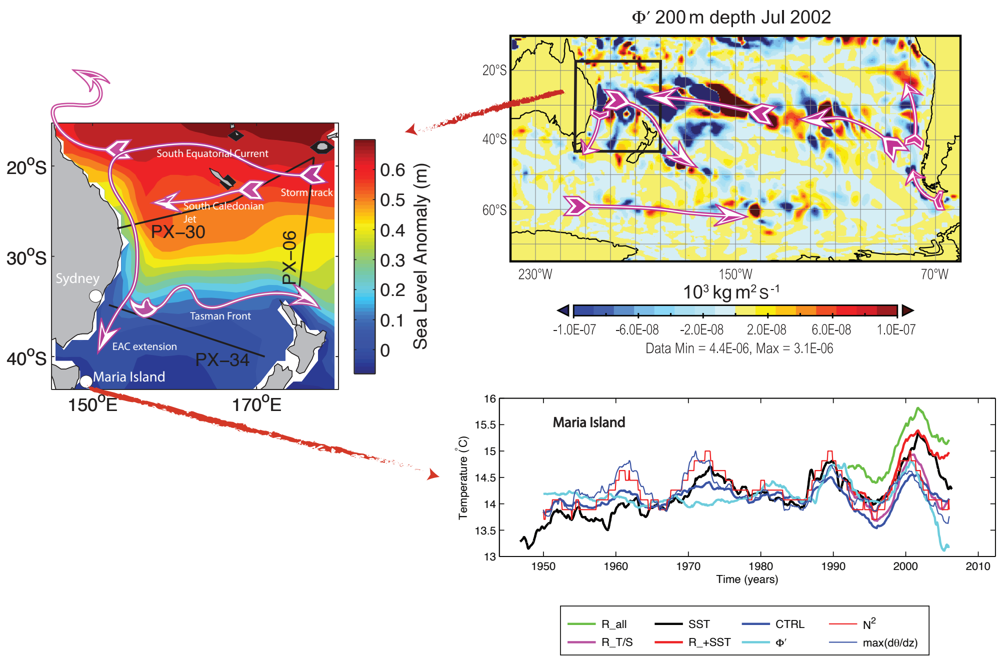

Figure 5. (left panel) Mean sea level (color) from the CTRL model (1950-2007), location of XBT lines, and schematic of major currents, (top right) Baroclinic Rossby wave disturbances, (bottom right) Temperature (°C) time series of the Maria Island station from in situ observations (SST) and free running model forced with reanalysed winds (CTRL), assimilating subsurface temperature and salinity profiles (R_T/S), including surface satellite sea surface temperatures (R_+SST) and with satellite sea surface height observations (R_ALL). CTRL has a 18°C bias correction applied. Φ' is the mean to transient potential energy conversion averaged over 150-350 m depth; N^2 is the Brunt-Vaisala (buoyancy) frequency averaged over 0-350 m depth; and max($d\theta/dz$) is the maximun of the vertical derivative of temperature describing the variability of the thermocline; N^2, and max($d\theta/dz$) are all calculated from the CTRL simulation and are normalized and scaled for comparison to the observed SST variability (black line).

the baroclinic energy conversion relating the energy transfer from the mean horizontal density gradients to the transients undergoes a major increase in amplitude post 1980. Sloyan and O'Kane (2014)[65] postulated that the strong correlations between the simulated and reanalysed ocean and the observed Maria Island SST suggest that the variability is strongly connected to the stability of the thermocline. They examined transport anomalies entering the East Australian Current at the Australian boundary and exiting via either the Tasman Front or the EAC Extension. This examination showed that periods of anomalously strong EAC transport at 25°S correspond to an anomalously strong Tasman Front and anomalously weak EAC-extension (see their Figures 15 & 16) and weaker stratification (N^2), smaller thermocline temperature gradients and energy conversion, and peaks in SST variability at Maria Island (see their Figure 17). Conversely, anomalously weaker EAC transport at 25°S correspond to an anomalously weaker Tasman Front and an anomalously stronger EAC-extension and stratification (N^2), larger thermocline temperature gradients and increased energy conversion. Taken together, their results show that Maria Island SST variability is fundamentally linked to baroclinic stability in the Tasman Sea which in turn is linked to the stability of the larger South Pacific ocean. In particular the dramatic change to the stability of the EAC post 1980 is seen to have a clear influence on the regions thermocline structure and on the component EAC currents and their associated transports.

4. The Stability of the High Latitude Southern Oceans and Sea Ice

O'Kane et al. (2013) [66] identified the Southern Ocean near the East Pacific Rise to be a key region where low frequency intrinsic variability arises largely due to topographic - baroclinic processes. Their simulations also described a nonlinear relationship between atmospheric forcing, thermocline ocean disturbances and sea-ice variability. Large scale coherent wave-trains of potential energy occur coincident with significant density gradients becoming topographically trapped in the region of the East Pacific Rise. In this region both baroclinic and barotropic instabilities were largest during the mature phase of regimes due to the combined effects of surface forcing related to SAM, ENSO and fast synoptics scale disturbances.

They showed how noise induced intrinsic variability may be amplified by either the low frequency SAM (zonal variations) and/or ENSO (latitudinal variations) modes of variability and that it is the Pacific sector of the Antarctic Circumpolar Currrent (ACC) where large scale intrinsic variability manifests most readily. They also found that high frequency winds (HFREQ) can further act to excite a significant internal ocean response in the Pacific, although weaker than that excited by either of the SAM or ENSO modes. Both the zonal SAM and HFREQ weather modes were able to generate wave-like anomalies in the SH mid-latitude oceans capable of propagation from the Pacific to the Atlantic sectors thereby establishing an oceanic teleconnection. However, only the weather modes were found to be capable of significant amplification of those disturbances upon reaching the Atlantic sector.

Importantly for the discussion here, the study [66] found that the low frequency variability observed in model simulations could be explained in terms of dynamical regimes. Once again applying FEM-BV-VARX to the three dimensional ocean, the time-series of regime affiliations was shown to have the frequency of the atmospheric forcing embedded in it with trends in the time of residence in each particular regime state. A pivot point indicating a fundamental change in the dynamics of the ocean-ice system was found to occur in the mid-1980s. The statistically significant trends observed in these component forcing experiments again reflects the marked decline in atmospheric SH mid-latitude blocking over the post 1978 period accompanied by the trend towards a more prevalent positive SAM phase [15]. This study showed that both the intrinsic and forced decadal modes of variability in the ACC could be associated with dynamical regimes which respond to systematic changes, not only in the dynamically relevant climate modes (SAM & ENSO), but also in response to systematic changes in the synoptic weather patterns. The SH mid-latitude oceans were shown to undergo a regime change lagging that which occurred in the SH mid-latitude atmosphere by about 5 years (figure 6). Further examination of a suite of experiments combining various components of the atmospheric forcing showed that this delay was mostly attributable to a lagged response due to the influence of ENSO at high latitudes. In figure 6 three composite states arising from forcing with bulk formulas derived from NOAA NCEP v1 reanalysis (CORE2) show large variability in the Pacific around 150°W-110°W. State 1 is largely unstructured, while states 2 and 3 have a similar pattern but of opposite sign. The most coherent response in the Atlantic sector occurs in states 2 and 3 with maxima/minima in the vacinity of 60°S 15°E. Coherent large scale structures also appear in the Pacific sector of the ACC but there are features throughout the entire circumpolar domain. The composites show the unstable region of intrinsic variability in the South Pacific is related to the South Atlantic Weak Mode (SAWM) region of the ACC with complex 3-state regime behaviour. Obvious trends are observed toward state 2 and away from states 1 and 3. Prior to 1980 all states in general exhibit little or no trend in residence length. The percentage time resident in any given state largely reflects the fact that between 1978 and 1988 there was a pivot point where the relative dominance of each dynamical regime state changes. The SAM and HFREQ pivot points occur almost coincidently with the 1970s atmospheric regime transition whereas the ENSO transition lags by about 7-10 years. The pivot point for the ocean regime transition occurs around 1984 lagging the atmosphere by 5 or so years.

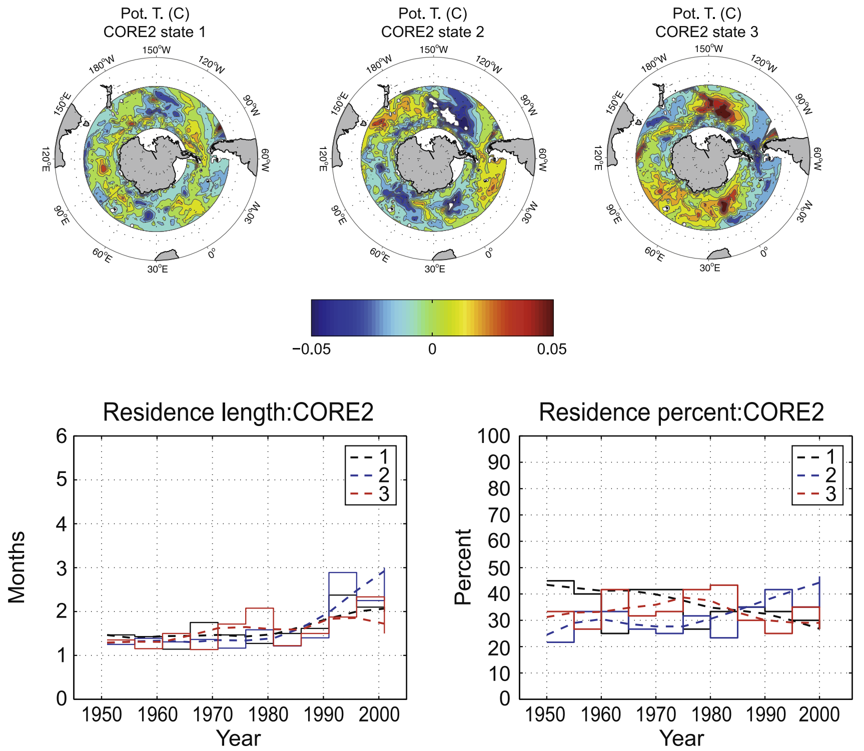

Figure 6. (Upper panels) FEM-BV-VARX cluster states at T200 dbars. Our analysis revealed three composite states arising from forcing the coupled ocean-ice model with bulk formulas derived from NOAA NCEP v1 reanalysis (CORE2). (Lower panels) Residence length (left panel) and percentage of time (right panel) spent in any given cluster state. The dashed lines are LOESS smoothed fits to the time averaged data. The values and averaging periods of the time averaged data are given by the solid lines.

This mechanisms by which ENSO variability is communicated to the higher latitudes remain to some extent controversial however, all invoke the influence of the Pacific South American mode [67]. Recently, it has been proposed that it is the thermal wind that communicates ENSO variability influencing the leading PSA mode (PSA1) [67] and that it is the combination of this mode and stochastic resonance induced by fast synoptic scale processes (PSA2) that induces a redened response in the South Pacific [68] completing an effective oceanic bridge between the tropics and extra-tropics.

Regime behaviour was further observed in sea ice formation about Antarctica. In figure 7, we show the leading 2 EOFs and PCs of ice concentration for various forcing combinations. Intrinsic variability generated by nominal year forcing plus small scale noise (CORE1 (1a and b)) reveals little variability outside of the Pacific. Given that the CORE1 atmospheric forcing has a significant noise component, it was concluded that sea-ice variability is more closely coupled to weather systems in this region. SAM variability (2a and b) associated with the zonal westerly winds enhances sea ice variability in the Ross and Weddell seas but most noticeably introduces sea-ice variability throughout the entire circumpolar region. Meridionally oriented latitudinal variations due to the PSA and ENSO (3a and b) induce a more coherent larger scale response in the Pacific amplifying the underlying intrinsic variability but only yield a marginal response in the Atlantic sector. Weather forcing (HFREQ not shown) induces coherent regions of large scale variability in both the Pacific and Atlantic regions of the Southern Ocean.The response to full interannual

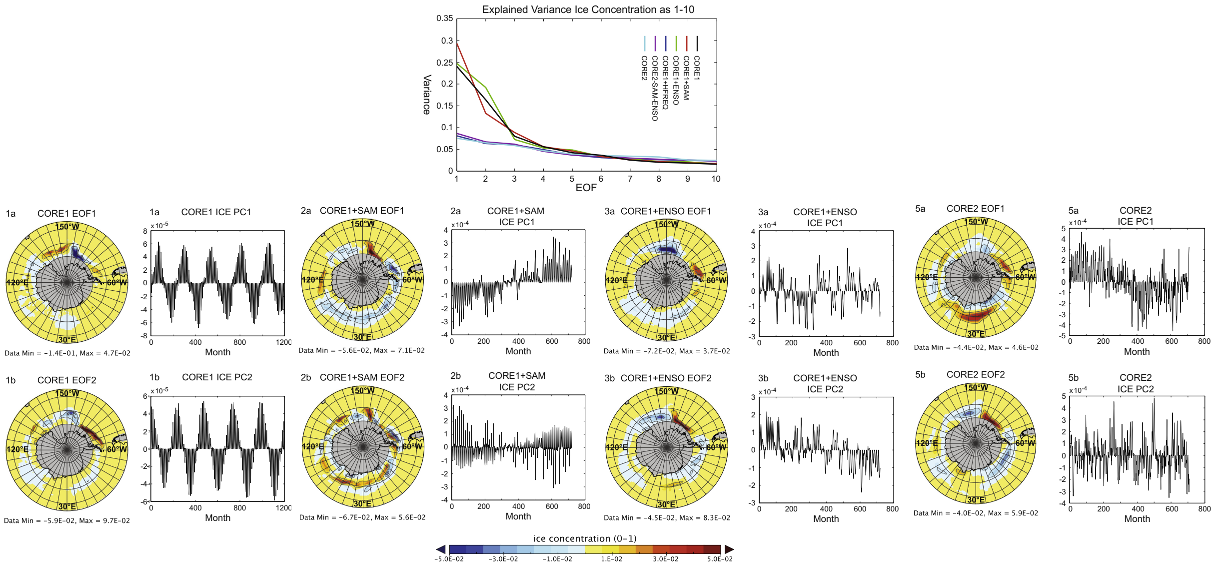

Figure 7. Leading 2 PCs of sea-ice concentration for forcing combinations. The CORE1 PCs (1a and b) exhibit decadal oscillations with a 20-year period which modulate the annual sea-ice cycle. SAM PC1 (2a) shows a distinct increasing trend which matches the observed SAM trend present in the reanalysed CORE2 data set. ENSO PCs (3a and b) show variability correlated with latitudinal variations in the atmospheric forcing. HFREQ PCs (not shown) display large scale low-frequency sea-ice variability coincident with the unstable regions of the subsurface ocean. The leading CORE2 PCs (5a and 5b) exhibit a less easily interpretable response with no clear relationship to the leading thermocline PCs and cannot simply be regarded as a linear combination of the constituent component experiments. The uppermost panel shows the explained variances as a percentage of the total for the leading 10 EOFs for ice concentration. The SAM, ENSO and CORE1 (intrinsic) component forcing experiments have steep slopes over the first 3 modes.

forcing (CORE2) can be reproduced using a linear combination of the aforementioned component responses. The CORE2 simulation regime affiliations show a clear transition between two dominant and one neutral regime states (figure 6) with the regime transition also reflected in at least one of the leading principal component (PC) timeseries for all of the forced sea ice simulations (figure 7) .

5. Spiciness Pathway

South Pacific subtropical density compensated temperature and salinity anomalies are known to be associated with equatorial thermocline variability. Disturbances generated in the eastern subtropics are advected towards the central equatorial Pacific ocean where they can directly modulate the thermocline [59,69,70]. Munk (1981) [71] first introduced the term "spiciness" to describe differences in the temperature (T) and salinity (S) of water of a given density on a given isopycnal surface. Tailleux et al. (2005) [72] formulated a general theory for such disturbances by which equatorward propagating subducted salinity anomalies amplify while their temperature counterparts are attenuated. To first order spiciness anomalies are both pressure and density compensated so that they are advected passively in the thermocline mean circulation from the eastern subtropics toward the tropics. It has now been recognised that the late 1970s transition to warmer tropical conditions [73] coincided with the arrival of a large-scale, subsurface cold and fresh water anomaly in the central tropical Pacific [59]. Developing an ocean reanalysis for the period 1990–2007

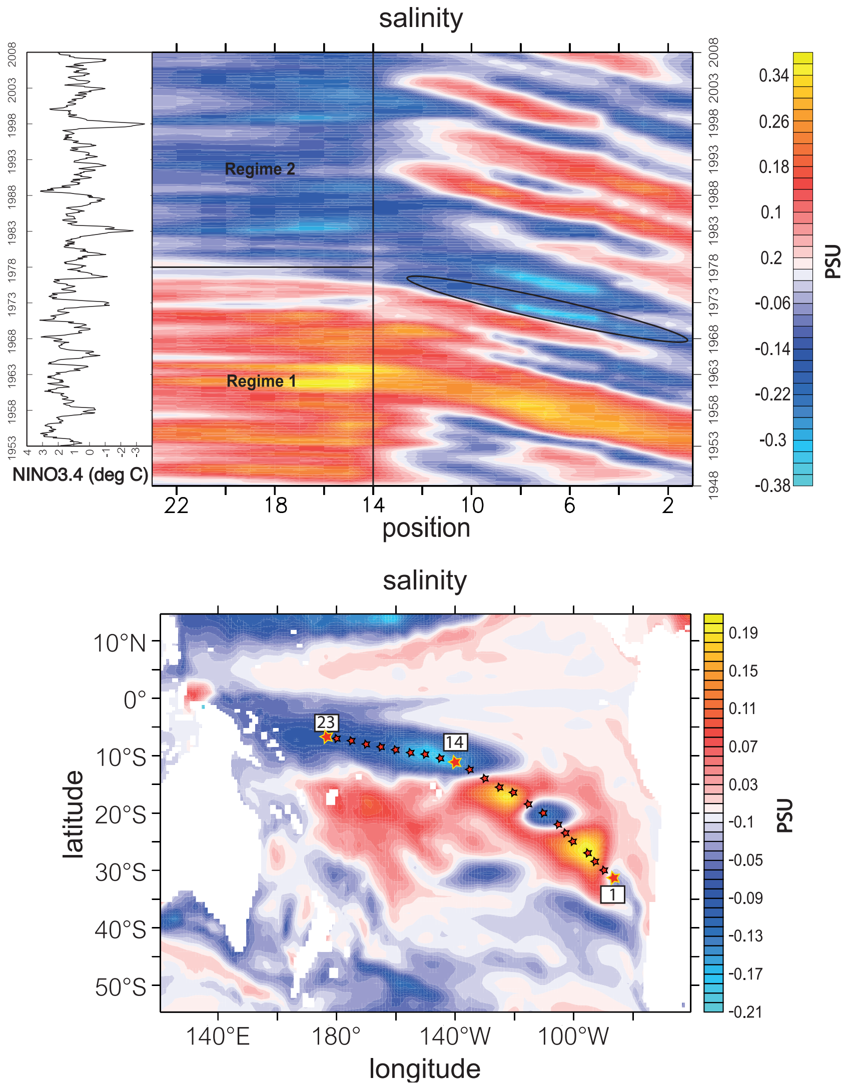

Figure 8. (upper panel) Hovmöller diagrams for anomalies along positions indicated in the lower panel. The trajectory of the 240 m salinity anomaly corresponding to the shoaling of the thermocline is indicated by the ellipse. The NINO3.4 index calculated from HadISST data is shown in the left panel insert. (lower panel) 240 m salinity (psu) anomalies on the 1st January 1990.

that assimilates subsurface Argo, XBT and CTD data, O'Kane et al. [59] showed that these anomalies occur due to the subduction of negative surface salinity anomalies from near 30°S, 100°W and are advected along the $\sigma = 25 - 26$ kg m^{-3} isopycnal surfaces. Taking about seven years to reach the central equatorial Pacific they may substantially perturb the thermocline before breaking up where the remnants of salinity ultimately ventilate in the region of the western Pacific warm pool. Spicy (warm and salty) disturbances, occur due to late winter diapycnal mixing and isopycnal outcropping, leading to subduction of subtropical mode waters and subsurface injection. On reaching the equatorial band (10° S–0° S) these disturbances tend to deepen the thermocline reducing the likelihood of large El Niño events occurring. In contrast the emergence of negative (cold–fresh) disturbances at the equator are associated with a shoaling of the thermocline and El Niño events.

We can now augment our previous discussion of the tropical Pacific thermocline regimes and SST variability in the following way:

- Regime 1 (Prior to 1978): A deepened western equatorial Pacific thermocline basic state and a more stably stratified (weakly stratified) density structure below (above) the thermocline. This is further associated with a warm–salty (cold– fresh) anomaly structure below (above) the thermocline.

- Regime 2 (Post 1978): A shallow western equatorial Pacific thermocline basic state and a more stably stratified (weakly stratified) density structure above (below) the thermocline. This is further associated with a cold–fresh (warm–salty) anomaly structure below (above) the thermocline.

6. Projections of the Future SH Climate

Coupled ocean - atmosphere - sea ice models are our primary tool for understanding the future climate and hence the lifetime of a given climatic regime. In order to have confidence in simulations of the future climate i.e., projections, it is important that climate models can realistically simulate the large scale teleconnections over the historical record, including the climatological storm tracks, during the twentieth century. While it is not reasonable to expect climate models to capture the observed occurrence and phases of specific teleconections e.g., El Niño, we do expect that they be at the very least able to accurately simulate the trends and variance of those teleconnections if not the observed causal relationships [74]. Frederiksen and colleagues tested the ability of successive programs of climate model development in simulating the observed austral winter changes in climatological baroclinicity and thereby storm tracks from CMIP3 [75] through to CMIP5 [36]. They found that most models simulated the changes in zonal wind, but only about a third of the models captured the observed changes in baroclinic instability and with reduced magnitude. The subset of models capable of simulating the observed spatial trends in the Phillips' Criterion and the associated changes in winter rainfall over southern Australia and especially in SWWA were used as a basis for a subsequent CMIP5 multi-model ensemble study conducted by Grainger et al. (2017) [76]. They found that the externally forced austral summer (DJF) variability in the Z^{500hPa} geopotential height resided almost exclusively in a SAM-like teleconnection with uniform positive loading in the tropics, extending to at least 30°S with an annular structure with negative loadings exhibited at higher latitudes. In the austral winter (JJA), they showed a similar teleconnection but displaced more equatorward with the largest annular loadings over southern Australasia, and especially over SWWA, consistent with a reduction in the zonal westerly wind near 30°S, and the observed reduction in baroclinity over the region. In both seasons, the slow external modes of variability were found to have a positive trend over the second half of the twentieth century reflecting the projected thermal expansion of the tropical troposphere and a poleward shift of the downward branch of the Hadley Cell.

Grainger et al. [76] further showed that for SWWA, the negative trend in rainfall was closely associated with the aforementioned annular pattern in Z^{500hPa} geopotential height, with positive height anomalies and anti-cyclonic flow at 300hPa over the region of decreasing rainfall. Frederiksen and Grainger (2015) [54] had earlier identified this same pattern in the leading slow external geopotential height mode of covariability in multi-model ensemble CMIP3 simulations and attributed this trend to external radiative forcing, including Greenhouse gases. An analysis over last 50 years of the twenty-first century in the RCP8.5 scenario [36] (figure 9), showed a similar slow external mode of covariability, but with an increasing downward trend in rainfall and upward trend in the positive height anomaly over SWWA, together with a much stronger anti-cyclonic circulation in the winds at 300hPa.

In figure 9, trends in RCP8.5 CMIP5 model projections are shown for the Phillips criterion and rainfall and the corresponding leading external modes for the austral summer and winter. Statistically significant trends $> 99.9\%$ confidence levels were found for the leading external mode, in each season, (DJF 0.90, JJA 0.85 $ms^{-1}year^{-1}$ respectively) with increased variance of the leading external mode were shown to be substantially larger than for simulations with observed historical radiative forcings. Frederiksen et al. (2017)[36] argue that the close similarity between the pattern of the projected trends and the horizontal structure of the external trend mode, with pattern correlations in DJF & JJA of 0.98 in both

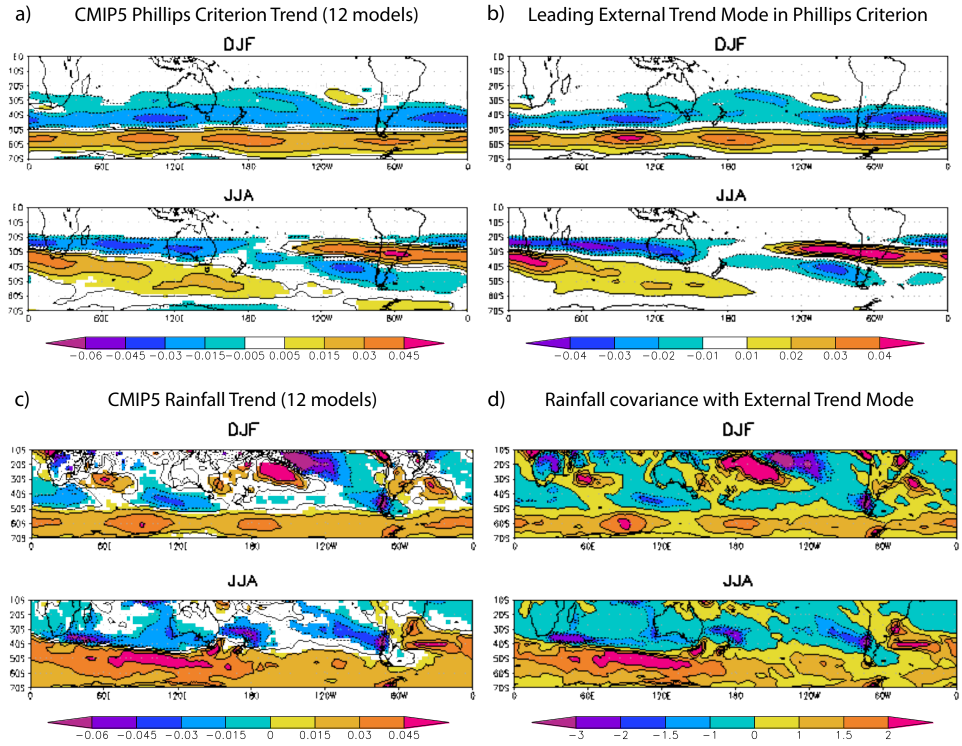

Figure 9. CMIP5 multi-model ensemble (2050-2099) trends in SH (a) Phillips Criterion (ms^{-1} year^{-1}) and (c) rainfall (mm day^{-1} year^{-1}) and the covariance between the external component of the (b) Phillips Criterion and (d) rainfall and the associated timeseries of leading external trend mode. Significant trends at the 95% level or greater are shaded. Figure modified from Frederiksen et al. (2017)[36].

seasons respectively, are an indication that the external forcing determines the trends in baroclinic instability and hence rainfall are largely due to anthropogenic greenhouse gases. A similar analysis with the RCP4.5 scenario, which has a pathway to stabilization over the last 50 years, showed a near complete collapse of this slow externally forced mode of covariability, indicating the importance of the continuing increase in Greenhouse gas forcing.

7. Summary and Conclusions

Identifying, let alone understanding regime behaviour in the broader climate system is clearly a considerable challenge. The challenges occur not simply because of the multiple timescales involved but due to the requirement that the observational network be continuous and of sufficient homogeneity in space and time across all of the domains of the system. In order to efficiently diagnose regime behaviour requires not only observations and model simulations but appropriate diagnostic tools for decomposing high dimensional, non-stationary and multiscale data. Here we have employed nonstationary temporally regularised clustering for regime identification alongside energetics and instability calculations and more standard methods of dimension reduction and decomposition such as singular spectral analysis, EOF/PCA, and vector auto-regressive methods. The import of applying analysis and modelling systems appropriate to the task cannot be underestimated.

Given the paucity of observations of the subsurface ocean prior to the advent of the Argo program, we must rely on model simulations to characterise the subsurface ocean. Where an ocean model can in part be constrained with surface forcing provided by atmospheric reanalysis there appears significant secular trends in the states of the South

Pacific, Southern Ocean and sea-ice around Antarctica over the decades since the 1950s. Here we have seen that systematic and rapid shifts in either the large scale components of the atmospheric circulation (SAM, ENSO) or changes in the frequency and persistence of synoptic scale features in atmospheric variability alone can initiate a regime change in SSTs, thermocline variability, oceanic baroclinic instability i.e. Rossby wave activity, sea-ice variability and spiciness disturbances. We have seen that tropical variability (ENSO) is communicated to the high latitudes by the atmosphere leading to a reddened oceanic response and that there exist dynamic oceanic pathways that feedback this response to in turn modify the background regime.

In combination, these studies show the complexity of the climate system and its response to changes across domains. In particular, they detail the dynamic oceanic response to systematic changes in the coherent structures of the troposphere via coherence resonance effects. These responses include impacts on sea ice variability and the energetics of the Southern Ocean. Positive reinforcement and feedbacks between the domains of the earth system are now manifest in the poleward shift of the tropospheric westerly winds being further enhanced via changes in meridional temperature gradients induced by a pronounced shift to warmer SSTs.

We propose that the SH climate system underwent a systematic regime shift in the late 1970s and early 1980s. Attribution studies of observational and reanalysis data [77] clearly show that this shift first occurred in the atmosphere primarily due to increasing rates of CO_2 exacerbated by seasonal O_3 mass deficit. The shift in tropospheric dynamics to a more SAM like summer circulation coincided with increased surface air temperatures, reduced storm formation and rainfall over southern Australia. The ocean responded with increasing thermocline, SST and baroclinic variability and instability in the EAC and generally warmer SSTs throughout the South Pacific. The imprint of the climate regime shift can even be seen in the high latitude upper ocean and sea-ice variability. Analysis of CMIP historical and projection simulations [36,54], consistent with the attribution study of Franzke et al. [22], point to CO2 emissions as the dominant driver of the late 1970s regime transition and that, without substantial reductions in CO2 emissions, the current regime dominated by a *SAM like* zonal state, a weakened subtropical jet and expanded tropics, will persist into the foreseeable future.

The relative paucity of observations in the SH has exacerbated the difficulty of first identifying and fully understanding this climate tipping point. It is only now, nearly 40 years after the transition that we can fully appreciate the impacts for the South Pacific and surrounds. If one were to consider similar changes in the mid-latitudes of the Northern Hemisphere, with comparable consequences for long term rainfall and temperatures then one could imagine enormous pressure would be placed on human systems. A final note of caution regarding CMIP projections relates to the huge uncertainties associated with the response of the Antarctic ice sheets and SH cryosphere to the circulation regime we now find ourselves in. Currently CMIP models do not have dynamic cryosphere model components and the relatively short observational record limits our understanding of even the natural variability of Antarctic glaciers and ocean - ice shelf interactions [78].

Author Contributions: Conceptualization, TJO and JSF; methodology, TJO, JSF, CSF, IH; software, TJO, JSF, CSF, IH; validation, TJO, JSF, CSF, IH; formal analysis, TJO, JSF, CSF, IH; investigation, TJO, JSF, CSF, IH; resources, TJO, JSF, CSF, IH; data curation, TJO, JSF, CSF, IH; writing—original draft preparation, TJO; writing—review and editing, TJO, JSF, CSF, IH; visualization, TJO, JSF, CSF, IH; supervision, TJO; project administration, TJO; funding acquisition,TJO, JSF, CSF, IH. All authors have read and agreed to the published version of the manuscript.

Funding: This research received no external funding.

Acknowledgments: TJO, JSF & CSF acknowldge the support of CSIRO.

Conflicts of Interest: The authors declare no conflict of interest.

Appendix A. FEM-BV-VARX Clustering

The Finite Element Bounded Variation Vector Auto-Regressive with eXternal factors (FEM-BV-VARX) method as applied to atmospheric reanalyses has been described in detail elsewhere [15,22,23] and is now well documented [14,79]. Here, we provide only a very brief outline of the method and refer interested readers to the citations provided. The FEM-BV-VARX analysis in the studies presented here, is typically applied to anomalies calculated as deviations from the climatological mean but without detrending, in order to preserve secular behaviours. The impact of reducing the dimensionality using principal component analysis (PCA) is to restrict the features present in the data dependent on the selection of fields and how the singular value decomposition is formulated. To this end a series of experiments needs to be undertaken to ascertain the sensitivity to retained dimensions and to how the covariances are constructed.

The general approach is to fit a non-stationary stochastic model to the data and to determine the optimal set of time evolving free model parameters. Let $\mathbf{x}_0, \ldots, \mathbf{x}_T \in \Psi \subset \mathbf{R}^n$ be the observed $n-$dimensional time series with $T+1$ daily averages in the interval $[0, T]$. Assuming that $\mathbf{x}_t$ can be approximated by the time-discrete output of a particular direct mathematical model $F[\mathbf{x}_t, \ldots, \mathbf{x}_{t-m\tau}, \theta(t), t] = 0$ where $F(\cdot)$ is the model operator, t is the model time step, $m\tau$ is the memory depth, and $\theta(t) : [0, T] \rightarrow \Omega \subset R^d$ is a (time-dependent) set of the model parameters with d the dimension of a model parameter space. Following the approach taken by [80] we next define a model distance functional (sometimes referred as a loss function) $g[\mathbf{x}_t, \theta(t)] : \Psi \times \Omega \rightarrow [0, \infty)$ describing the distance (or loss) between some given $\mathbf{x}_t$ at time t and the output of the model $F(\cdot)$ calculated for a fixed set of parameters $\theta(t)$. For a given observation series $\mathbf{x}_0, \ldots, \mathbf{x}_T$ and some fixed functional form $g(\cdot)$, the inverse problem (or the parameter identification problem) can be approached via the solution of the following variational problem:

$$\sum_{t=1}^{T} g[\mathbf{x}_t, \theta(t)] \rightarrow min\theta(t) \tag{A1}$$

subjected to the constraints given above.

The problem as it stands is ill posed and so requires some assumptions to be made about the temporal dependence of the unknown parameters $\theta(t)$. Following [80,81], we now assume that for any $t \in [0, T]$ model distance, functional $g[\mathbf{x}_t, \theta(t)]$ can be represented as a convex linear combination of $K \geq 1$ stationary model distance functionals i.e. model functionals, dependent on some constant (time-independent) model parameters $\theta_i \in \Omega, i = 1, \ldots, K$ such that

$$g[\mathbf{x}_t, \theta(t)] = \sum_{i=1}^{K} \gamma_i(t) g(\mathbf{x}_t, \theta_i) \tag{A2}$$

with some convex set of time-dependent model affiliations $\gamma_i(t)$, i.e.

$$\sum_{i=1}^{K} \gamma_i(t) = 1, \quad \forall t \in [0, T], \tag{A3}$$

$$\gamma_i(t) \geq 0, \quad \forall t \in [0, T], \quad i = 1, \ldots, K \tag{A4}$$

and where we define $\Theta = \theta_1, \ldots, \theta_K$. The assumption here is that at any time t the global time-dependent (or nonstationary) model distance functional $g[\mathbf{x}_t, \theta(t)] : \Psi \times \Omega \rightarrow [0, \infty)$ can be approximated by one of K local time-independent (or stationary) model distance functionals chosen according to some time-dependent probabilities (or model affiliations) $\Gamma = [\gamma_1(t), \ldots, \gamma_K(t)]$.

The FEM-BV-VARX approximates dynamical processes by a stochastic model of the form:

$$\mathbf{x}_t = \mu_t + \mathbf{A}(t)\phi_1(\mathbf{x}_{t-\tau}, \ldots, \mathbf{x}_{t-m\tau}) + \mathbf{B}(t)\phi_2(u_t) + \mathbf{C}(t)\epsilon_t \tag{A5}$$

where more specifically $\Theta = (\mu(t), \mathbf{A}(t), \mathbf{B}(t), \mathbf{C}(t))$ is the vector of time dependent model parameters with mean $\mu(t)$. ϕ_1 is in general a nonlinear function connecting present and past observations $(\mathbf{x}_{t-\tau}, \ldots, \mathbf{x}_{t-m\tau})$, but here we take it to be the linear autoregressive factor model - adopting the perspective of Granger causality (that dwells on stationary autoregressive models) [7]. $\phi_2(u_t)$ is an external factor function, and $\mathbf{C}(t)$ couples the non-parametric, independent and identicallly-distributed (i.i.d.) noise process ϵ_t to the analysed time series (hereby modelling the impact of unresolved subgrid-scale effects). Time dependence of the model parameters Θ is also induced by the influence of the unresolved scales - and leads to regime transitions in many realistic systems.

For a given number, K, of clusters and fixed maximal time lag, m, the method minimises the distance of the model trajectory (of model metric g) at each time, t, to one of K model clusters. The model metric used is the Euclidean norm measuring the model error as the squared distance between $\mathbf{x}_t$ and the output of the average model function $g(\mathbf{x}_t, \theta(t)) = ||\mathbf{x}_t - \mu(t) - \mathbf{A}(t)\phi_1(\mathbf{x}_{t-\tau}, \ldots, \mathbf{x}_{t-m\tau}) - \mathbf{B}(t)\phi_2[u(t)]||_2^2$ (see [81] for details). We explicitly compare results for time lags corresponding to Bernoulli (random memoryless: lag 0), Markovian (dependent only on the prior timestep: lag 1) and non-Markovian (long term memory effects - here we consider memory out to 4 days: lags 2–4). The model affiliation sequence

$$\Gamma = \gamma_1(t), \gamma_2(t), \ldots, \gamma_K(t) \tag{A6}$$

represents the probabilities of residing in each cluster state. The time-dependent vector $\Gamma = (\gamma_1(t), \ldots, \gamma_K(t))$ contains the probabilities for an observation x_t at time t to be described/explained by an output of a vector autoregressive external factor model (VARX) with constant (time-independent) model parameters θ_i. Γ together with $\Theta = \theta_1, \ldots, \theta_K$ are jointly obtained from the numerical optimisation given by Equation A7. The method treats the clustering of non-stationary multidimensional data, $\mathbf{x}_t \in \mathbf{R}^d$ as a minimisation problem:

$$L(\Theta, \Gamma) = \sum_{t=0}^{T} \sum_{i=1}^{K} \gamma_i(t) g(\mathbf{x}_t, u_t, \theta_i) \rightarrow min(\Gamma, \Theta) \tag{A7}$$

subject to convexity constraints $\sum_{i=1}^{K} \gamma_i(t) = 1, \forall t \in [0, T]$ and $\gamma_i(t) \geq 0, \forall t \in [0, T], i = 1, \ldots, K$.

The number of different spatio-temporal regimes/clusters K, the model parameters to be chosen within these regimes, such as memory depth and number of PCs, and the indicator functions $\gamma_k(\cdot)$ signalling activation of the respective model regimes, are all determined simultaneously in a global optimisation procedure. This yields a judicious compromise between low residuals in reproducing the data of a training set on the one hand, and the demand for the smallest-possible overall number of free parameters of the complete model on the other. The resulting FEM-BV-framework is essentially nonparametric and parameter free, apart from the overall number of optimisation repetitions (annealing steps) with different randomly-chosen initial values Γ or Θ for parameter optimisation. Increasing this number reduces the probability of getting trapped in one of the local minima of L (for $N_C > 0$), simultaneously linearly increasing the amount of computations. Therefore, the number of annealing steps should be chosen carefully, dependent on the available computational resources and the size of the data to be analysed.

The optimisation problem is now solved by a finite element approach (see [79,80,82] for more information and a detailed description of the algorithm) using principal components of the EOFs as described in [62]. The persistency constraint C bounds the persistency of the function γ_i via the norm

$$|\gamma_i|_{BV(0,T)} = \sum_{t=0}^{T-1} |\gamma_i(t+1) - \gamma_i(t)| = \|D\gamma_i^{\dagger}\|_1 \leq C, \tag{A8}$$
$$D = \begin{bmatrix} -1 & 1 & \dots & 0 \\ 0 & -1 & \dots & 0 \\ \dots & \dots & \dots & \dots \\ 0 & \dots & -1 & 1 \end{bmatrix},$$

where $i = 1, \dots, K$, the scalar persistency parameter C measures the maximal number of transition between the local model i and all other models in the time interval $(0, T)$, $\gamma_i = [\gamma_i(1), \dots, \gamma_i(T)] \in \mathbf{R}^T$, $\dagger$ is the transposition operation and $\| \cdot \|_1$ is the 1-norm.

In context of nonstationary inference, it is appropriate to use the AIC to determine the right order parameters of the VARX model, i.e. the memory depth m, the number of cluster K and the optimal BV-persistency C [80]. To select the proper order parameters (and the optimal functional for external factors $\phi_2[u_t]$ in Equation A5) for a given persistency parameter value (Equation 18 [81] [1]), the AIC is defined as

$$AIC = -2 \log L_{max} + 2M, \tag{A9}$$

where L_{max} is the maximum log likelihood achievable by the model and M is the number of free parameters. The lowest AIC is preferred. It should however be appreciated that AIC can only be applied to discriminate between models of a given dimension. Thus the AIC can only determine the optimal choice of model parameters (including penalizing for ill-conditioning and overfitting) for a given class of stochastic model with the same fixed number of PCs (dimensions) but whose retained memory information may vary. It therefore follows that information theoretic methods cannot discriminate between models whose parameters have different dimensions, i.e. different retained number of PCs.

A key output of the FEM-BV-VARX method is the posterior model affiliation sequence (or Viterbi path) describing the most likely cluster state, i, of the system at each time. From the Viterbi path, one can construct composites by averaging the anomalous data instances $\mathbf{x}_t$ over all times when the system is in each of the respective regime states corresponding to the cluster states $i = 1, \dots, K$. Composites of the original data show the spatial structure of each (metastable) cluster state. The Viterbi path also allows a construction of the residence behaviour of the system in switching between each cluster state and allows for the identification of secular trends in each of the regime states. The resulting optimal Viterbi path provides a natural method for generating the climatology of a particular cluster state sequence. Cluster states are constructed by first assigning a model affiliation to each data point in the time-series of anomalies according to the Viterbi path or model affiliation sequence $\mathbf{\Gamma}$. Then all anomalies for each given cluster state assignation are averaged. The averaged state is the composite or meta-stable cluster state.

1. Dijkstra, H.A. Numerical bifurcation methods applied to climate models: Analysis beyond simulation. *Nonlinear Processes Geophys.* **2019**, *26*, 359–369.
2. Lenton, T.M.; Rockström, J.; Gaffney, O.; Rahmstorf, S.; Richardson, K.; Steffen, W.; Schellnhuber, H.J. Climate tipping points -Too risky to bet against. *Nature* **2019**, *575*, 592–595.
3. Yan, P.; Feng, G.; Hou, W.; Yang, P. A method for predicting the uncompleted climate transition process. *Nonlinear Processes Geophys.* **2020**, *27*, 489–500.
4. Kypke, K.L.; Langford, W.F.; Willms, A.R. Anthropocene climate bifurcation. *Nonlinear Processes Geophys.* **2020**, *27*, 391–409.
5. Australian Academy of Science. The Risks to Australia of a 3°C Warmer World, 2021.

[1] For a complete description of the persistency parameter formulation see section 2d of [81].

6. Frederiksen, J.S.; Osbrough, S.L. Tipping Points and Changes in Australian Climate and Extremes. *Climate* **2022**, *10*, 73. https://doi.org/10.3390/cli10050073.
7. Granger, C.W.J. Investigating Causal Relations by Econometric Models and Cross-spectral Methods. *Econometrica* **1969**, *37*, 424–438. https://doi.org/10.2307/1912791.
8. Sugihara, G.; May, R.; Hao, Y.; Chih-hao, H.; Deyle, E. Detecting Causality in Complex Ecosystems. *Science* **1969**, *338*, 496–500. https://doi.org/10.1126/science.1227079.
9. Horenko, I. Cheap robust learning of data anomalies with analytically solvable entropic outlier sparsification. *PNAS* **2022**, *119*, e2119659119. https://doi.org/10.1073/pnas.211965911.
10. Horenko, I. On a Scalable Entropic Breaching of the Overfitting Barrier for Small Data Problems in Machine Learning. *Neural Computation* **2020**, *132*, 1563–1579. https://doi.org/10.1162/neco_a_01296.
11. Vecchi, E.; Pospišil, L.; Albrecht, S.; O'Kane, T.J.; Horenko, I. eSPA+: Scalable Entropy-Optimal Machine Learning Classification for Small Data Problems. *Neural Computation* **2022**, *119*, e2119659119. https://doi.org/10.1073/pnas.211965911.
12. Horenko, I.; Vecchi, E.; Kardoš, J.; Wächter, A.; Schenk, O.; O'Kane, T.J.; Gagliardini, P.; Gerber, S. On cheap entropy-sparsified regression learning. *PNAS* **2022**, *120*, e221497212. https://doi.org/10.1073/pnas.2214972120.
13. Horenko, I. Nonstationarity in multifactor models of discrete jump processes, memory and application to cloud modeling. *J. Atmos. Sci.* **2011**, *68*, 1493–1506.
14. Metzner, P.; Putzig, L.; Horenko, I. Analysis of persistent nonstationary time series and applications. *Comm. Appl. Math. Comp. Sci.* **2012**, *7*, 175–229.
15. O'Kane, T.J.; Risbey, J.S.; Franzke, C.L.E.; Horenko, I.; Monselesan, D.P. Changes in the Metastability of the Midlatitude Southern Hemisphere Circulation and the Utility of Nonstationary Cluster Analysis and Split-Flow Blocking Indices as Diagnostic Tools. *J. Atmos. Sci.* **2013**, *70*, 824–842.
16. Vercauteren, N.; Klein, R. A clustering method to characterize intermittent bursts of turbulence and interaction with submesoscale motions in the stable boundary layer. *Journal of the Atmospheric Sciences* **2014**, *72*, 1504–1517. https://doi.org/10.1175/JAS-D-14-0115.1.
17. Marques, R.F.C.; Rao, V.B. Interannual variations of blocking in the Southern Hemisphere,. *J. Geophys. Res.* **2000**, *105*, 4625–4636.
18. Frederiksen, J.S.; Frederiksen, C.S. Interdecadal changes in southern hemisphere winter storm track modes. *Tellus A* **2007**, *59*, 599–617.
19. Wiedenmann, J.M.; Lupo, A.R.; Mokhov, I.I.; Tikhonova, E.A. The climatology of blocking anti-cyclones for the Northern and Southern Hemispheres: Block Intensity as a diagnostic. *J.Climate* **2002**, *15*, 3459–3473.
20. van Loon, H.; Jenne, R.L. The zonal harmonic standing waves in the Southern Hemisphere. *J. Geophys. Res.* **2002**, *77*, 992–1003.
21. Trenberth, K.E.; Mo, K.C. Blocking in the Southern Hemisphere. *Mon. Weather Rev.* **2002**, *113*, 3–21.
22. Franzke, C.L.E.; O'Kane, T.J.; Monselesan, D.P.; Risbey, J.S.; Horenko, I. Systematic attribution of observed Southern Hemispheric circulation trends to external forcing and internal variability. *Nonlin. Processes Geophys.* **2015**, *2*, 675–707.
23. O'Kane, T.J.; Risbey, J.S.; Monselesan, D.P.; Horenko, I.; Franzke, C.L.E. On the dynamics of persistent states and their secular trends in the waveguides of the Southern Hemisphere troposphere. *Climate Dynamics* **2016**, *46*, 3567–35973.
24. Frederiksen, J.S.; Frederiksen, C.S. Decadal Changes in Southern Hemisphere Winter Cyclogenesis. *CSIRO Marine and Atmospheric Research Paper; CSIRO: Melbourne, Australia* **2005**, *2*, p29.
25. Frederiksen, J.S.; Frederiksen, C.S. Twentieth Century Winter Changes in Southern Hemisphere Synoptic Weather Modes. *Adv. Meteorol.* **2011**, p. 353829.
26. Osbrough, S.L.; Frederiksen, J.S. Interdecadal changes in Southern Hemisphere winter explosive storms and Southern Australian rainfall. *Climate Dynamics* **2021**, *56*, 3103–3130.
27. Corti, S.; Molteni, F.; Palmer, T.N. Signature of recent climate change in frequencies of natural atmospheric circulation regimes. *Nature* **1999**, *398*, 799–802.
28. Kobayashi, S.; Ota, Y.; Harada, Y.; Ebita, A.; Moriya, M.; Onoda, H.; Onogi, K.; Kamahori, H.; Koboyashi, C.; Endo, H.; et al. The JRA-55 Reanalysis: General Specifications and Basic Characteristics. *Journal of the Meteorological Society of Japan. Ser. II* **2015**, *93*, 5–48. https://doi.org/10.2151/jmsj.2015-001.
29. Kalnay, E.; coauthors. The NCEP/NCAR 40-Year Re-analysis Project. *Bull. Amer. Meteor. Soc.* **1996**, *77*, 437–471. https://doi.org/10.1175/1520-0477(1996)077,0437:TNYRP.2.0.CO;2.
30. O'Kane, T.J.; Monselesan, D.P.; Risbey, J.S.; Horenko, I.; Franzke, C.L.E. On memory, dimension, and atmospheric teleconnections. *Math. Clim. Weather Forecast.* **2017**, *3*, 1–27.
31. Arblaster, J.M.; Meehl, G.A. Contributions of External Forcings to Southern Annular Mode Trends. *J. Climate* **2006**, *19*, 2896–2905.
32. Turner, J.; Comiso, J.C.; Marshall, G.J.; Lachlan-Cope, T.A.; Bracegirdle, T.; Maksym, T. Non-annular atmospheric circulation change induced by stratospheric ozone depletion and its role in the recent increase of Antarctic sea ice extent. *Geophys.Res. Lett.* **2009**, *36*, L08502. https://doi.org/10.1029/2009GL037524.
33. Son, S.W.; Gerber, E.P.; Perlwitz, J.; Polvani, L.M.; Gillett, N.P.; Seo, K.H.; et al. Impact of stratospheric ozone on Southern Hemisphere circulation change: A multimodel assessment. *J. Geophys. Res.* **1999**, *115*, D00M07. https://doi.org/10.1029/2010JD014271.
34. Previdi, M.; Polvani, L.M. Climate system response to stratospheric ozone depletion and recovery. *Q. J. Roy. Meteorol. Soc.* **2014**, *140*, 2401–2419. https://doi.org/10.1002/qj.2330.

35. Barnes, E.A.; Barnes, N.W.; Polvani, L.M. Delayed Southern Hemisphere climate change induced by stratospheric ozone recovery, as projected by the CMIP5 models. *J. Climate* **2013**, *276*, 852–867.
36. Frederiksen, C.S.; Frederiksen, J.S.; Sisson, J.; Osbrough, S.L. Trends and projections of Southern Hemisphere baroclinicity: the role of external forcing and impact on Australian rainfall. *Climate Dynamics* **2017**, *48*, 3261–3282. https://doi.org/10.1007/s00382-016-3263-8.
37. Trenberth, K.E. Storm tracks in the Southern Hemisphere. *J. Atmos.Sci.* **1991**, *48*, 2159–2178.
38. Steele, L.P.; Krummel, P.B.; Langenfelds, R.L. Atmospheric CO2 concentrations from sites in the CSIRO Atmospheric Research GASLAB air sampling network (August 2007 version), Trends Compend, Data Global Change Carbon Dioxide. *Inf. Anal. Cent., Natl. Lab., US Dep. Energy, Oak Ridge TN, USA,* **2007**.
39. Skeie, R.B.; Berntsen, T.K.; Myhre, G.; Tanaka, K.; Kvalevåg, M.M.; Hoyle, C.R. Anthropogenic radiative forcing time series from pre-industrial times until 2010. *Atmos. Chem. Phys.* **2011**, *11*, 11827–11857. https://doi.org/10.5194/acp-11-11827-2011.
40. Bourassa, A.E. Large volcanic aerosol load in the stratosphere linked to Asian monsoon transport. *Science* **2011**, *337*, 78–82.
41. Fröhlich, C. Observations of irradiance variations. *Space Sci. Rev.* **2000**, *94*, 15–24.
42. Roscoe, H.K.; Haigh, J.D. Influences of ozone depletion, the solar cycle and the QBO on the Southern Annular Mode. *Q. J.Roy. Meteorol. Soc.* **2007**, *133*, 1855–1864.
43. Parzen, E.; Tanabe, K.; Kitagawa, G., Eds. *Information Theory and an Extension of the Maximum Likelihood Principle: Selected Papers of Hirotugu Akaike*; Springer, 1988.
44. Cowtan, K.; Way, R.G. Coverage bias in the HadCRUT4 temperature series and its impact on recent temperature trends. *Q. J.Roy. Meteorol. Soc.* **2014**, *140*, 1935–1944.
45. Lee, S.; Feldstein, S.B. Detecting Ozone- and Greenhouse Gas-Driven Wind Trends with Observational Data. *Science* **2013**, *339*, 563–567.
46. Freitas, A.C.V.; Frederiksen, J.S.; Whelan, J.; O'Kane, T.J.; Ambrizzi, T. Observed and simulated inter-decadal changes in the structure of Southern Hemisphere large-scale circulation. *Climate Dynamics* **2015**, *45*, 2993–3017.
47. Saji, N.H.; Goswami, B.N.; Vinayachandran, P.N.; Yamagata, T. A dipole mode in the tropical Indian Ocean. *Nature* **1999**, *401*, 360–363.
48. Mo, K.C. Relationships between Low-Frequency Variability in the Southern Hemisphere and Sea Surface Temperature Anomalies. *J. Climate* **2000**, *13*, 3599–3610.
49. Troup, A.J. The 'Southern Oscillation'. *Q. J. Roy. Met. Soc.* **1965**, *91*, 490–506.
50. Gallant, A.J.E.; Hennessy, K.J.; Risbey, J. Trends in rainfall indices for six Australian regions: 1910–2005. *Aust. Meteorol. Mag.* **2007**, *56*, 223–239.
51. Hendon, H.; Thompson, D.; Wheeler, M. Australian Rainfall and Surface Temperature Variations Associated with the Southern Hemisphere Annular Mode. *J. Climate* **2007**, *20*, 2452–2467.
52. Ummenhofer, C.C.; England, M.H.; McIntosh, P.C.; Meyers, G.A.; Pook, M.J.; Risbey, J.S.; Gupta, A.S.; Taschetto, A.S. What causes southeast Australia's worst droughts? *Geophys. Res. Lett.* **2009**, *36*, L04706.
53. Cai, W.; Cowan, T.; Sullivan, A. Recent unprecedented skewness towards positive Indian Ocean Dipole occurrences and its impact on Australian rainfall. *Geophys. Res. Lett.* **2009**, *36*, L11705.
54. Frederiksen, C.S.; Grainger, S. The role of external forcing in prolonged trends in Australian rainfall. *Climate Dynamics* **2015**, *45*, 2455–2468. https://doi.org/10.1007/s00382-015-2482-8.
55. Dey, R.; Lewis, S.; Abram, N.; Arblaster, J. A review of past and projected changes in Australia's rainfall. *Wiley Interdiscip. Rev.Clim. Chang.* **2015**, *10*, e557.
56. Phillips, N.A. Energy Transformations and Meridional Circulations associated with simple Baroclinic Waves in a two-level,Quasi-geostrophic Model. *Tellus* **2002**, *6*, 273–286.
57. Frederiksen, C.S.; Frederiksen, J.S. A theoretical model of Australian Northwest cloud band disturbances and Southern Hemisphere storm tracks: The role of SSTs. *J. Atmos. Sci.* **1996**, *49*, 1410–1432.
58. Risbey, J.S.; P. C. McIntosh, M.J.P. Synoptic components of rainfall variability and trends in southeast Australia. *Int. J. Climatology* **2013**, *33*, 2459–2472.
59. O'Kane, T.J.; Matear, R.J.; Chamberlain, M.A.; Oke, P.R. ENSO regimes and the late 1970s climate shift: The role of synoptic weather and South Pacific ocean spiciness. *J. Comp. Phys.* **2014**, *271*, 19–38.
60. Lou, J.; O'Kane, T.J.; Holbrook, N.J. A Linear Inverse Model of Tropical and South Pacific Seasonal Predictability. *J. Climate* **2020**, *33*, 4537–4554. https://doi.org/10.1175/JCLI-D-19-0548.1.
61. O'Kane, T.J.; et al.. CAFE60v1: A 60-Year Large Ensemble Climate Reanalysis. Part II: Evaluation. *J. Climate* **20201**, *34*, 5171–5194.
62. Horenko, I. On Simultaneous Data-Based Dimension Reduction and Hidden Phase Identification. *J. Atmos. Sci* **2008**, *65*, 1941–1954.
63. O'Kane, T.J.; Matear, R.J.; A.Chamberlain, M.; Oliver, E.C.J.; J.Holbrook, N. Storm tracks in the Southern Hemisphere subtropical oceans. *J. Geophys. Res. Oceans* **2014**, *119*, 6078–6100. https://doi.org/10.1002/2014JC009990.
64. Chapman, C.C.; Sloyan, B.M.; O'Kane, T.J.; Chamberlain, M.A. Interannual Subtropical Indian Ocean Variability due to Long Baroclinic Planetary Waves. *J. Geophys. Res. Oceans* **2020**, *33*, 6765–6791. https://doi.org/10.1175/JCLI-D-19-0469.1.
65. Sloyan, B.M.; O'Kane, T.J. Drivers of decadal variability in theTasman Sea. *J. Geophys. Res. Oceans* **2014**, *120*, 1–18. https://doi.org/10.1002/2014JC010550.

66. O'Kane, T.J.; Matear, R.J.; Chamberlain, M.A.; Risbey, J.S.; Sloyan, B.M.; Horenko, I. Decadal variability in an OGCM Southern Ocean: Intrinsic modes, forced modes and metastable states. *Ocean Modelling* **2013**, *69*, 1–21. https://doi.org/10.1016/j.ocemod.2013.04.009.
67. O'Kane, T.J.; Monselesan, D.P.; Risbey, J.S. A multiscale re-examination of the Pacific South American pattern. *Mon. Wea. Rev.* **2017**, *145*, 379–402.
68. Lou, J.; O'Kane, T.J.; Holbrook, N.J. Linking the atmospheric Pacific-South American mode with oceanic variability and predictability. *Communications Earth and Environment* **2021**, pp. 1–8. https://doi.org//10.1038/s43247-021-00295-4.
69. Nonaka, M.; Sasaki, H. Formation mechanism for isopycnal temperature-salinity anomalies propagating from the eastern South Pacific to the equatorial region. *J. Climate* **2007**, *20*, 1305–1315.
70. Kolodziejczyk, N.; Gaillard, F. Variability of the heat and salt budget in the subtropical southeastern Pacific mixed layer between 2004 and 2010: Spice injection mechanism. *J. Phys. Oceanogr.* **2013**, *43*, 1880–1898.
71. Munk, W. Internal waves and small scale processes. *Evolution of Physical Oceanography* **1981**, *MIT Press*.
72. Tailleux, A.; Lazar, A.; Reason, C. Physics and dynamics of density-compensated temperature and salinity anomalies. Part 1: Theory. *J. Phys. Oceanogr.* **2005**, *35*, 849–864.
73. Giese, B.; Urizar, S.; Fuckar, N. Southern hemisphere origins of the 1976 climate shift. *Geophys. Res. Lett.* **2002**, *29*, 1014.
74. Harries, D.; O'Kane, T.J. Dynamic Bayesian networks forevaluation of Granger causal relationships in climate reanalyses. *Journal of Advances in Modeling Earth Systems* **2021**, *13*, e2020MS0024420. https://doi.org/10.1029/2020MS002442.
75. Frederiksen, C.S.; Frederiksen, J.S.; Sisson, J.; Osbrough, S.L. Changes and Projections in Australian Winter Rainfall and Circulation: Anthropogenic Forcing and Internal Variability. *Int. J. Clim. Chang.* **2011**, *2*, 143–162. https://doi.org/10.18848/1835-7156/CGP/v02i03/37071.
76. Grainger, S.; Frederiksen, C.S.; Zheng, X. Projections of Southern Hemisphere atmospheric circulation interannual variability. *Climate Dynamics* **2017**, *48*, 1187–1211. https://doi.org/10.1007/s00382-016-3135-2.
77. Franzke, C.; Horenko, I.; Majda, A.J.; Klein, R. Systematic Metastable Atmospheric Regime Identification in an AGCM. *J. Atmos. Sci* **2009**, *66*, 1997–2012.
78. Gwyther, D.E.; O'Kane, T.J.; Galton-Fenzi, B.K.; Monselesan, D.P.; Greenbaum, J.S. Intrinsic processes drive variability in basal melting of the Totten Glacier Ice Shelf. *Nature Communications* **2018**, *9*, 3141. https://doi.org/10.1038/s41467-018-05618-2.
79. Horenko, I. On robust estimation of low-frequency variability trends in discrete Markovian sequences of atmospheric circulation patterns. *J. of Atmos. Sci.* **2009**, *66(11)*, 1941–1954.
80. Horenko, I. Finite element approach to clustering of multidimensional time series. *SIAM J. Sci. Comput.* **2010**, *32*, 62–83.
81. Horenko, I. On the identification of nonstationary factor models and their application to atmospheric data sets. *J. Atmos. Sci.* **2010**, *67*, 1559–1574.
82. Horenko, I. On clustering of non-stationary meteorological time series. *Dynamics of Atmospheres and Oceans* **2010**, *49*, 164–187.